

The Origin of the Dual-Slope Spectrum from Intermediate to Transitional Scale in Equatorial Spread F

F. S. Kuo and S. Y. Chou

*Institute of Space Science, National Central University,
Chung-Li, Taiwan 320, R.O.C.*

(Received August 16, 2001)

Horizontal spectra of equatorial bubble-irregularities generated by numerical simulations are systematically investigated. We found that a bubble with smooth structure grows in the bottom-side ionosphere due to Gravitational Rayleigh-Taylor (GRT) instabilities, and breaks into an irregular structure in the topside ionosphere to form a system of bubble-irregularities. A smooth waveform of the density fluctuations will be obtained from a horizontal cut through the smooth structure of the bubble, while an irregular waveform will be obtained if a horizontal cut through the irregular structure of the bubble is made. The power spectra of the smooth waveform are always steep with spectral index $-3 \gg -6$, and the spectra of the irregular waveform are shallow with spectral index $-1.5 \gg -2$. This characteristic is found to be universal, regardless of the scale size of the system of bubble-irregularities. Considering the relative detection-probability, we argue that a satellite passing through the topside ionosphere will most likely encounter irregular waveforms of the primary bubble-irregularities (larger scale) with shallow spectrum, and smooth waveforms of the secondary bubbles (small scale) with steeper spectrum. One example of satellite data of IPEI on board ROCSAT-1 is examined and explained, based on these simulation results.

PACS. 94.20.Ji – F region.

PACS. 94.20.Lk – Topside region.

I. Introduction

Power law spectra are mostly formed at the saturation stage of some nonlinear processes. Kolmogorov [1] pioneered this problem in his neutral turbulence theory, which states that, if a neutral fluid in an isotropic homogeneous medium is stirred at some wave number k_0 , structure will form and energy will cascade to smaller scale structure creating a whole spectrum following a $k_i^{-5/3}$ power law. The cascade will cease at some wave number k_m due to molecular viscosity leading to a break of the spectrum at k_m . Scores of power law universal spectra have been reported in the earth environment since then. A well-known example among them is the universal gravity wave spectrum in the ocean [2-4] and in the lower atmosphere [5-7]. The vertical wave number spectrum ($\gg k_i^{-3}$) of gravity waves at saturation in the atmosphere is explained by dynamic instability and energy cascade in the wind shear [8, 9]. The theory states that a gravity wave (GW) propagating upward in the wind field will be trapped in the region of dynamic instability, where the horizontal phase velocity matches the wind velocity, and the GW will gain energy from the background wind through wave-shear interaction. When the wave amplitude grows to a limit,

it starts to break and cascade energy to smaller scale structure to form a power law spectrum, until some eddy diffusion process becomes effective to break it. From these observations, we can say that a power law spectrum is basically formed out of the balance between energy input (instabilities) and energy output (dissipations) and the redistribution of energy through nonlinear processes. Therefore, precise estimates of the spectral indices are essential, since any attempt to apply any non-linear theory to the observations will depend upon matching the indices to certain characteristic scaling numbers.

The wave number spectrum of equatorial spread F extends from global scales down to short wavelengths as small as 10 cm, covering 7 orders of magnitude. Consequently, the study of spread F irregularities has been divided into various wavelength sub-ranges: planetary (> 1000 km), medium (10-1000 km), intermediate (0.1-10 km), transitional (10-100 m), and short wavelength (< 10 m) [10]. Observations of the spectrum of spread F irregularities in the sub-ranges of intermediate scale and transitional scale basically fall into two categories: measurements on board satellites [11-15] and measurements on board rockets [10, 16-21]. Satellite-borne probes allow measurement of the horizontal-, and the rocket-borne instrumentation observes the vertical-wave number spectrum. Very often, the spectrum of the observed density fluctuation takes the form of a power law, i.e., $I_k \propto k^{-\alpha}$. The spectral index α typically lies between $\alpha \approx 1.5$ and $\alpha \approx 2.5$ in the intermediate scale [10-13, 15, 17, 19, 21], and between $\alpha \approx 4$ and $\alpha \approx 5$ in the transitional scale [10, 15, 20, 21]. It is suggested that either low-frequency electrostatic drift waves at high altitude (> 280 km) [10, 20], or a one-dimensional nonlinear convective steepening associated with the collisional interchange instability [22], may cause the break in the slope of the power spectrum.

Numerical simulation [23, 24] has also been applied to investigate the wave number spectrum of equatorial spread F for the intermediate scale. The one dimensional wave number spectrum, deduced from the simulations in the developed nonlinear state, invariably takes the power law form with spectral index $\alpha \approx 2.5 \pm 0.5$. It is important to note that no (2-D) simulation has ever identified the mechanism of the break in the slope of power spectrum from the intermediate to transitional scale. In this paper, we will present a study of the wave number spectrum of the system of bubble-irregularities in the sub-ranges of intermediate and transitional scale by simulations. It covers about 4 orders of magnitude in wave length from 2.5 m to 25 km. We understand that it is unrealistic to try a single two-dimensional simulation to cover the whole range of the spectrum from the intermediate to the transitional scale because it would need hundreds of millions of grid points. So, we decided to simulate the bubble-irregularities of large and small scales independently. The main object of this study is to identify the origin of the break in the slope of the ESF wave number spectrum. Then an example of IPEI data obtained by the instruments on board Taiwan satellite ROCSAT-1 will be examined and compared with the simulations.

II. Numerical model

The model used in this study is the same as that of previous studies of irregularities in the equatorial F region ionosphere [25-27]. The set of equations that are solved is a subset of the full governing equations. They consist of the continuity equation of the plasma,

$$\frac{\partial n}{\partial t} + \nabla \cdot (nV_e) = 0; \quad (1)$$

the steady state electron and ion velocity equations,

$$\mathbf{V}_e = \mathbf{E} \times \mathbf{B} / B^2; \quad (2)$$

$$\mathbf{V}_i = \frac{\mathbf{E}}{B} + \frac{\mathbf{g}}{-\omega_i} + \frac{\mathbf{v}_{in}}{-\omega_i} \quad \mathbf{E} \times \frac{\mathbf{B}}{B} + \frac{\mathbf{v}_{in}}{-\omega_i} \frac{\mathbf{E}}{B} + \frac{\mathbf{g}}{-\omega_i} + \frac{\mathbf{v}_{in}}{-\omega_i} \quad \left(1 + \frac{\mu \omega_{in}}{-\omega_i} \right)^{-1}; \quad (3)$$

and the equation for the quasi-neutrality condition,

$$\mathbf{r} \cdot \mathbf{J} = 0; \quad (4)$$

where $\mathbf{J} = n_e(\mathbf{V}_i - \mathbf{V}_e)$ is the current density; n is the number density of the plasma; B is the amplitude of the magnetic field \mathbf{B} ; ω_{in} , ω_i , \mathbf{E} , \mathbf{g} , \mathbf{v}_{in} , \mathbf{V}_i , and \mathbf{V}_e are the ion-neutral collision frequency, ion gyro-frequency, electric field, gravitational acceleration, neutral wind velocity, ion and electron velocities, respectively. The background conditions of all the simulations in this paper are generally the same as that of our previous studies [27, 28] unless specified. A constant magnetic field B_0 of 0.25 G is pointed northward, the gravitational force is pointed downward (negative Z direction), and the neutral wind is $\mathbf{v}_{in} = 0$. The ion neutral collision frequency ω_{in} is assumed to decrease with height from 2.0 to 0.01 s^{-1} in the height range between 250 and 530 km, as shown in right hand panel of Fig. 1. The background electron density is assumed to increase exponentially with height in the range between bottom-height Z_b and the peak-density-height Z_p , and decrease with height in the range between Z_p and the top-height Z_t . The three heights Z_b , Z_p , and Z_t are the parameters to be assigned in each simulation, case by case. One example with $Z_b = 250$ km, $Z_p = 430$ km, and $Z_t = 534$ km is shown in the left hand panel of Fig. 1, in which the largest vertical gradient of the density profile appears at 390 km altitude with a 10 km scale length. Correspondingly, the horizontal range of simulation L_x , the grid sizes Δx , Δz and the time step size Δt are also specified case by case. The numerical scheme of computation in this study is also the same as in our previous studies: The flux-corrected transport (FCT) algorithm [29, 30] has been applied to carry out the time integration of the continuity equation (1); and the successive-over-relaxation (SOR) technique is applied to solve the quasi-neutrality equation (4). At the beginning of each simulation, a 5% density perturbation is superposed on the background profile.

III. Results

Four cases of simulations will be presented: three of them (Cases L1, L2, L3) deal with a larger scale primary system of bubble-irregularities and one (Case S1) deals with a smaller scale secondary system of bubble-irregularities. For the convenience of discussion, we call the bubble growing from the bottom-side ionosphere due to a GRT instability as the primary bubble, and the bubble growing from the interior of the primary bubble is called the secondary bubble of the first-generation. The primary bubble will break into an irregular structure when it penetrates into the topside ionosphere, and the secondary bubble will break into an irregular structure at the wall of the primary bubble. Similarly, the bubble growing from the interior of a secondary bubble of the first generation is called the secondary bubble of the second generation, and so forth. The geometric parameters of the baseline simulations are listed in Table I. One can see that the

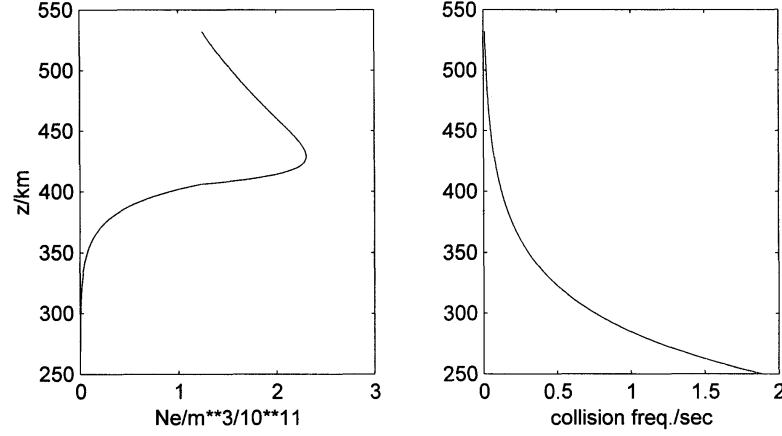


FIG. 1. (Left panel): Background electron density profile with the lower boundary at $z_b = 250$ km, the upper boundary at $z_t = 534$ km, and the density peak at the altitude of $z_p = 430$ km. (Right panel): Ion neutral collision frequency profile for all the simulations.

TABLE I. Geometrical parameters of the baseline simulations

	Case L1	Case L2	Case L3	Case S1
Horizontal simulation range	25 km	12.5 km	6.25 km	125 m
Vertical simulation range	284 km	284 km	284 km	2.84 km
Bottom altitude z_b	250 km	250 km	250 km	450 km
Top altitude z_t	534 km	534 km	534 km	452.84 km
Density peak altitude z_p	430 km	430 km	430 km	451.27 km
Horizontal grid size Δx	250 m	125 m	62.5 m	1.25 m
Vertical grid size Δz	1 km	0.5 km	0.25 km	5 m
Grid resolution $N_x \times N_z$	100 \times 283	100 \times 565	100 \times 1129	100 \times 565
Time step size Δt	0.05 s	0.025s	0.0125 s	0.125 ms

largest horizontal scale-length ($\Delta L_x = 25$ km of Case L1) and the smallest horizontal scale-length ($\Delta L_x = 2.5$ m of Case S1) of the bubble-irregularities are separated by 4 orders of magnitude in wave number.

III-1. Spectral analysis of a primary system of bubble-irregularities

Fig. 2 shows, from left to right, the snapshots of the density contours of Cases L1 \gg L3 at saturation stage. We say that a simulation is at the saturation stage if the horizontal spreading of the irregularities has stretched to the limit of the horizontal simulation range. The three cases

show a common feature, as described in [27] in detail: The bubble starts to grow smoothly from the bottom-side ionosphere due to the GRT instability, and will break into an irregular structure in the topside ionosphere due to the combining force of upward pushing from below and downward pressing from above the bubble. The upwelling bubble in the bottom-side ionosphere has a smooth structure, because there is no restoring force to counter the $\mathbf{E} \times \mathbf{B}$ upwelling force. For the convenience of discussion again, we define three clearly identifiable regions in each case: The region below the lowest rightward-arrow is identified as the first smooth bubble region (SB1 or growing bubble) and the region between the lower two rightward-arrows is identified as the second smooth bubble region (SB2 or steepening bubble); the region between the upper two rightward-arrows in each panel of Fig. 2 is identified as the irregular bubble region (IB). The exact ranges of these regions are listed in Table II. Examples of the density variation of the one-dimensional horizontal cuts through certain heights of the bubble of Case L2 are demonstrated in Fig. 3. Diagrams (a) and (b) are sampled cuts from the region of SB1; Diagrams (c) and (d) are sampled from the region of SB2, and Diagrams (e) » (i) are from the region of IB. The altitude (in km) of the horizontal cut is denoted in each diagram. Clearly, the horizontal density variation has a smooth waveform in the region SB1, and the smooth waveform is steepened in the region of SB2. In the region IB, the waveform of the horizontal density variation is totally irregular.

We have Fourier-analyzed the normalized density fluctuation $\pm n = hni$ of each height at saturation to obtain the power densities I_k of each Fourier mode:

$$\frac{\pm n(x; z)}{hni} = \sum_{k=1}^{\infty} A_k(z) \cos \frac{2\pi kx}{L_x} + B_k(z) \sin \frac{2\pi kx}{L_x}; \quad (6a)$$

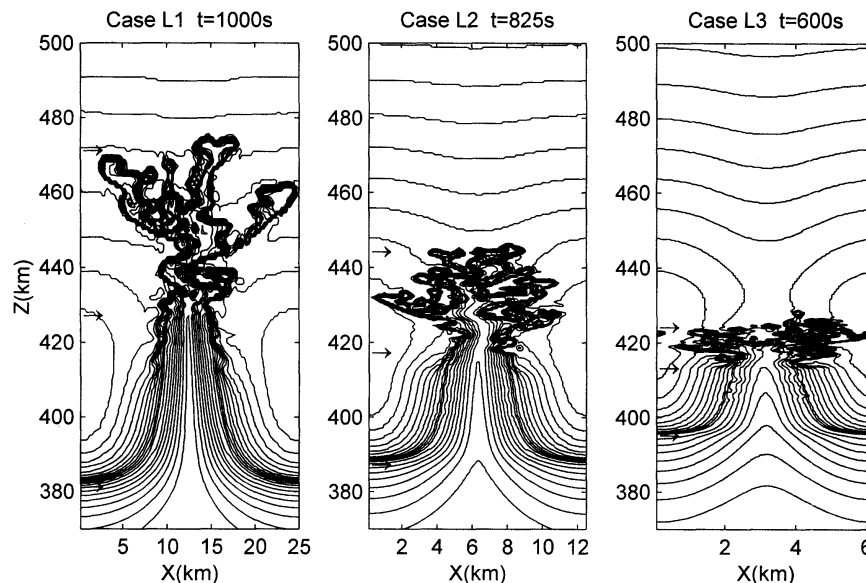


FIG. 2. Snapshots of the density contours of Case L1 at 1000 sec (left panel), Case L2 at 825 sec (middle panel), and Case L3 at 600 sec (right panel). The rightward-arrows indicate the boundaries of the irregular structures and the smooth structures of the bubble-irregularities.

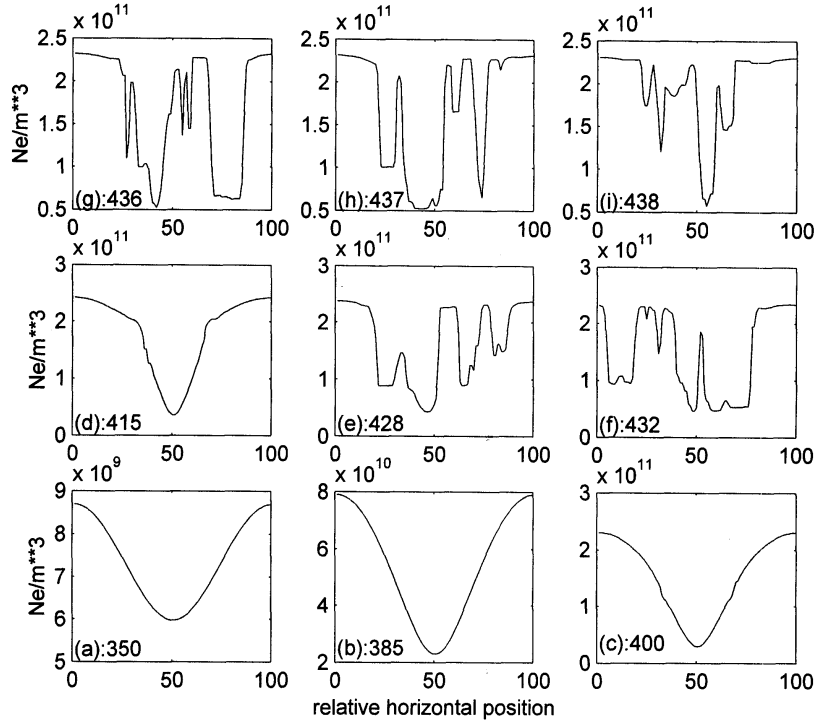


FIG. 3. Examples of the density variation of the one-dimensional horizontal cuts through certain heights of the bubble of Case L2. Diagrams (a) and (b) are sampled cuts from the SB1 region; Diagrams (c) and (d) are sampled from the SB2 region, and Diagrams (e) » (i) are from the IB region. The number denoted in the left-lower corner of each diagram is the altitude in terms of kilometers.

TABLE II. Parameters of the irregular bubble region and smooth bubble regions

	Case L1	Case L2	Case L3
Height range of SB1 (km)	250 » 381	250 » 386	250 » 393
Height range of SB2 (km)	381 » 428	386 » 416	393 » 411
Height range of IB (km)	428 » 469	416 » 440	411 » 422
Thickness of SB1: ζZ_{SB1} (km)	131	136	143
Thickness of SB2: ζZ_{SB2} (km)	47	30	18
Thickness of IB: ζZ_{IB} (km)	41	24	11
Ratio $\zeta Z_{IB} = (\zeta Z_{SB1} + \zeta Z_{SB2})$	0.23	0.145	0.068

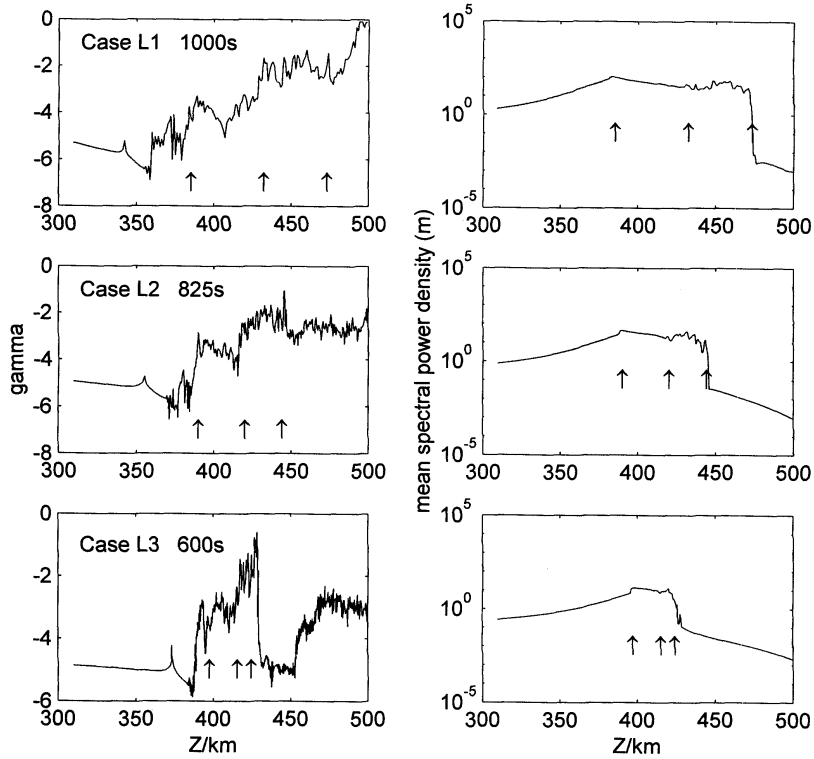


FIG. 4. Spectral power index γ (left panels) and the mean spectral power density (right panels) as functions of height. (Top panels): Case L1 at 1000 sec; (Middle panels): Case L2 at 825 sec; and (Bottom panels): Case L3 at 600 sec. The up arrows shown in each panel indicate the boundaries of the irregular structure and smooth structure of the primary bubble-irregularities system.

$$I_k = \frac{(A_k^2 + B_k^2) \langle L_x \rangle}{2^k}, \tag{6b}$$

where $L_x = \langle x \rangle N_x$ is the horizontal scale length of the simulation under analysis, $\langle n \rangle$ represents the average density and $\pm n = n_j - \langle n \rangle$ is the density fluctuation of the corresponding height. Since there is 100 grid points in each height, we have 50 Fourier modes. We take the power densities I_k of the first 24 modes ($k = 1 \dots 24$) for spectral analysis by least square-fitting them to a power law:

$$I_k = \langle n \rangle \epsilon k^\alpha \tag{7a}$$

The mean spectral power density is defined as:

$$\langle n \rangle = \frac{1}{24} \sum_{k=1}^{24} I_k \tag{7b}$$

The results of the spectral analysis for cases L1, L2, and L3 are summarized from top to bottom, respectively, in Fig. 4, where the three left-hand panels display the height dependence of spectral power index α , and the three right-hand panels display the mean spectral power density as functions of height. The upward-arrows shown in each panel are the counterparts of the corresponding rightward arrows in Fig. 2 indicating the boundaries of irregular bubble region and smooth bubble regions. One can see that the spectral index α of each height is between α_1 and α_2 in the irregular bubble region (IB), and between α_3 and α_4 in the second smooth bubble region (SB2). The mean spectral energy densities of each height in the IB and SB2 regions are approximately equal. In the height range of SB1, the mean spectral energy density slowly decreases with distance away from SB2, and the spectrum is steeper with spectral index α between α_4 and α_6 . In the height range above IB, the mean spectral energy density sharply drops to such a low level that its power spectra look like noise with small spectral index.

The transitions from SB1 to SB2 and from SB2 to IB, as shown in Fig. 4, are the consequences of the process of the upwelling of the plasma bubble: The bubble starts at some altitude in the bottom-side ionosphere and grows up due to the GRT instability, more and more plasma will join the bubble as it wells-up toward topside ionosphere. So, in this region (SB1), the total fluctuation energy grows with height, because the bubble consists of more plasma at higher altitudes, and the spectral index doesn't change because the bubble's shape doesn't change. In the region SB2, the bubble keeps welling up and steepening, with very little new plasma joining. The steepening of the bubble will make fluctuation energy flow from large scales to small scales, so the averaged spectral energy density of the first 24 Fourier modes slowly decreases with height, and the spectral index α jumps from $\alpha_4 \gg \alpha_6$ in the region of SB1 to $\alpha_3 \gg \alpha_4$ in the region of SB2. When the bubble penetrate into the topside ionosphere, as explained in [27], it starts to break into an irregular structure, accelerating the energy flow from large scales to small scales. So in the region of IB, the averaged spectral energy density of the first 24 Fourier modes decreases further, and the spectral index α also jumps from $\alpha_3 \gg \alpha_4$ in the SB2 region to $\alpha_1 \gg \alpha_2$.

III-2. Simulation and analysis of a secondary system of bubble-irregularities

When the primary bubble wells upward from the bottom-side into the topside ionosphere, the density gradient of the leading edge on the top of the bubble will increase sharply, because of the squeezing by the upward $E \times B$ pushing from below and the downward restoring force pressing from above [27]. The local theory of the GRT instability [28] suggests that small perturbations can grow much faster than the primary bubble, due to the much sharper density gradient on the leading edge of the primary bubble. We will present one example of simulation (Case S1) of a secondary bubble using the imagined density profile shown in Fig. 5, where the normalized background density profile for the cases L1 \gg L3 is also displayed for comparison. Note that the grid-resolutions of Case L2 and Case S1 are the same, with $100 \leq 565$, while the vertical grid sizes of Case L2 and S1 are 500 m and 5 m, respectively (see Table II). Therefore, it can be seen from Fig. 5 that the amplitude of the density gradient below the density peak in the case S1 is 100 times larger, and the amplitude of the density gradient above the density peak is about 30 times larger, than the corresponding part in the cases L1 \gg L3. The simulation has reached saturation at simulation time $t = 8s$, its density contour (not shown) is similar to that of Fig. 2, and the behavior of the corresponding power spectra (not shown) is also similar to that of Fig. 4, as expected. The similarity between the secondary bubble-irregularities and the primary bubble-irregularities is demonstrated in Fig. 6, which shows the density power spectra averaged over

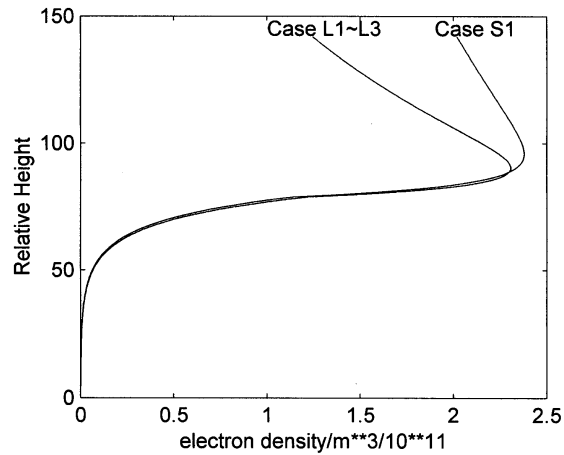


FIG. 5. Background electron density profile for the simulation of Case S1. The corresponding density profile for Cases L1 » L3 (Fig. 1) is mapped proportionally to this figure for comparison. Note that the grid-resolutions of Case L2 and Case S1 are the same, with $100 \text{ \AA} \times 565$, while the vertical grid sizes of Case L1 and S1 are 125 m and 1.25 m respectively. Therefore, the amplitude of density gradient below the density peak in the case S1 is 100 times larger, and the amplitude of density gradient above the density peak is about 30 times larger than the corresponding part in the cases L1 » L3.

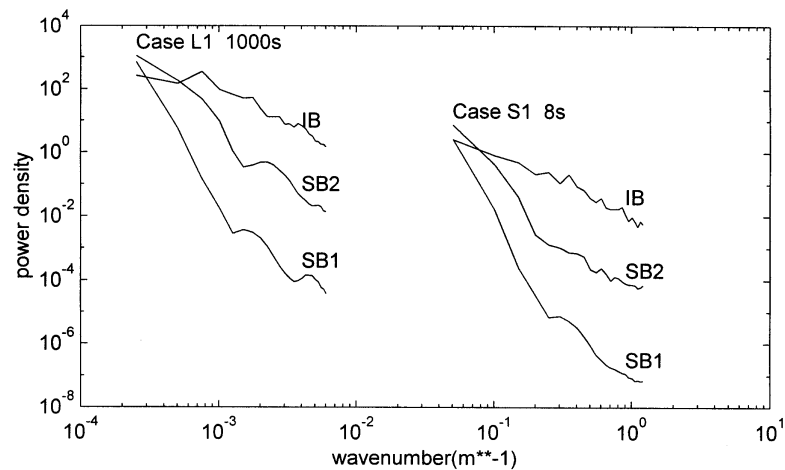


FIG. 6. Averaged density power spectra in the IB, SBI and SB2 regions for the cases L1 and S1. The spectra of the two systems are clearly similar.

many heights in the IB, SB1 and SB2 regions for the cases L1 and S1. Such self-similar scale invariance, that is, the small-scale structuring is reminiscent in form of the large-scale structuring and of the structuring at all scales in between, had been reported experimentally [16, 31]. The self-similar scale invariance is important in understanding the transitional spectra of the ESF and will be discussed. It is important to mention here that, in all the simulations, we have totally

ignored the finite ion Larmor radius effects (FLR effects), which may affect the Rayleigh-Taylor instability at small scales. We shall come back to discuss this point later.

III-3. Implication of simulation results on the wave number spectra of ESF

With these results of the simulations, we are ready to construct a picture of the horizontal wave number spectra of the ESF obtained by satellite in-situ measurement, such as the IPEI on board satellite ROCSAT-1 [15]. Our simulations reveal a universal behavior of the system of bubble-irregularities in the F-region ionosphere: 1. The spectral index α is $\alpha \approx 1$ in the IB region, $\alpha \approx 3$ in the SB2 region, and $\alpha \approx 6$ in the SB1 region regardless of the scale size of the system, and the average spectral energy density is proportional to the horizontal scale size. The penetration depth into the topside ionosphere increases with increasing horizontal scale size of the bubble-irregularities (see Fig. 2 and Table II). 2. The interior of the primary bubble-irregularities is a GRT instability region for secondary bubbles to grow. And the secondary bubble will break into an irregular structure when it penetrates through the top walls of the primary bubble, where the density gradient is the highest and turns from upward into downward in a very small height range. These results imply that the relative probability of seeing a small scale irregular structure is smaller than that of seeing the large scale irregular structure by satellite, because of the scale size dependence of the penetration depth; also, the probability of seeing smooth structure rather than seeing irregular structure increases with decreasing scale size. So we expect the satellite to see a spectrum with spectral index α being $\alpha \approx 1$ at large scale, and $\alpha \approx 3$ at smaller scale when it passes through an ESF region.

IV. Interpretation of in-situ measurements of the energy spectra of the ESF

Su *et al.* (1999) [15] had reported a power spectrum inside a bubble observed by IPEI. The Ionospheric Plasma and Electrodynamics Instrument (IPEI) on board ROCSAT-1 is designed to measure the ion composition, density, temperature and drift velocity at the 600 km altitude along the ROCSAT-1 orbit within the latitude band of 35^\pm [32]. The spectrum they reported is obtained from the data of 0325 ~ 0327 UT on March 28, 1999 (which will be referred as data set SU hereafter), when the IPEI operated at Fast Mode to sample data at 1024 Hz during the passage of bubble events. The reported power spectral density of the electron density fluctuation had been broken into three sections according to the definition given in [10]- medium scale (10 ~ 1000 km), intermediate scale (0.1 ~ 10 km), and transitional scale (10 ~ 100 m), to fit f_k / k^α separately to obtain the spectral indexes, $\alpha_1 = 1.3$, $\alpha_2 = 2.1$, and $\alpha_3 = 4.4$.

IV-1. Electron density fluctuation

Data set SU includes two separate bubble events: the first event is clearly stronger than the second event. In order to compare with our results of simulations, we decided to re-examine the spectrum of the first bubble event (data between 3:25:17 and 3:25:50 within data set SU). Samples of the electron density as a function of flight time observed by satellite are demonstrated in Fig. 7. The time resolution of this data set is 1s/1024 (fast mode), corresponding to a horizontal range resolution of 7 meters approximately. It can be seen that many smooth waveforms with scale length less than 100 meters are clearly identifiable as indicated by the arrows. These smooth waveforms are very similar to the waveforms in the SB1 and SB2 regions obtained by simulations (see Fig. 3a-d). One can also see that the waveforms at large scales are very irregular. We found

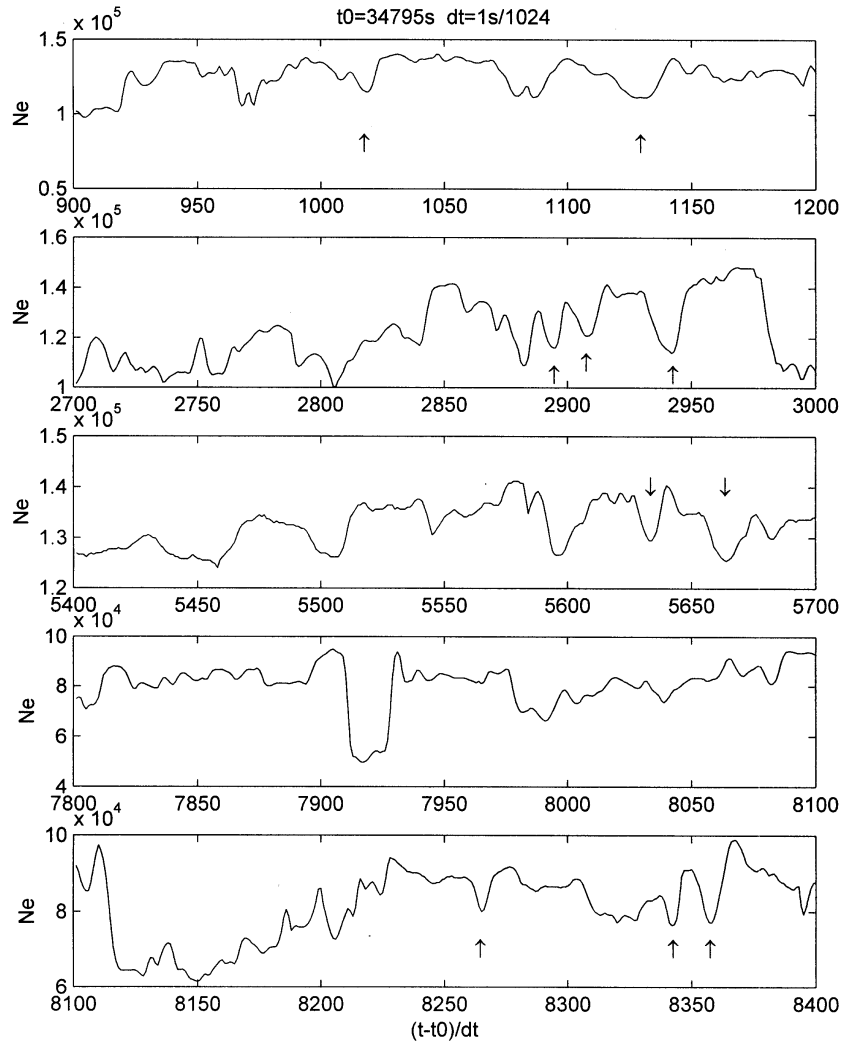


FIG. 7. Samples of electron density as a function of flight time t observed by satellite. The time resolution of this data set is $dt = 1s/1024$ (fast mode), corresponding to a horizontal range resolution of 7 meters approximately. The referenced parameters t_0 and dt for the horizontal axes are given on the top of this figure. Arrows indicate the smooth waveforms of small scales.

that, after examining many bubble events, the smooth waveforms at small scale and irregular waveforms at large scale, as shown in Fig. 7, are a common feature observed by the ROCSAT-1 satellite. To analyze the characteristics of the power spectrum, we take the first 8001 data points of the electron density starting from the first data point, then transform each density n_i into the density fluctuation $\pm n_i - \bar{n} = (n_i - \bar{n})/\bar{n}$, where \bar{n} is the average of these 8001 densities. After subtracting the linear trend of the series $f \pm n_i - \bar{n} g$, we make a Fourier transform of the data series to obtain a power spectrum. Then we shift the data series rightward by 400 points, i.e., take the next 8001 points starting from the 401st point, and make the spectral analysis to obtain the second

spectrum. We repeat the procedures of shifting and analysis until the end of the bubble event, a total number of 67 spectra are obtained and their average is shown in Fig. 8. This averaged spectrum extends from the left end at the wavelength of around 50 km to the right end at around 30 m, containing the three scaling sections defined in [10]. We apply the same criterion to analyze the behavior of the spectral index of Fig. 8: Take 400 consecutive Fourier modes to fit the power law $I_k \propto k^\alpha$, and shift 40 modes rightward to calculate the spectral index α of another section until the end of the spectrum. The dependence of the spectral index α on the wave-number k is shown in Fig. 9, where the α value of each section is assigned to its first Fourier mode. For example, the spectral index α of the section between $k = 0.0186$ ($\lambda = 338$ m, indicated by the upward-arrow) and $k = 0.069$ ($\lambda = 91$ m, indicated by the downward-arrow) is assigned to $k = 0.0186$. Fig. 9 clearly reveals that the spectral indexes of the corresponding wave numbers $k \cdot 0.0186$ are uniformly distributed around $5/3$, and the α values for $k > 0.069$ continuously decrease with increasing k from $\alpha \approx 2.7$ to $\alpha \approx 4.2$. This behavior of spectral index can be explained based on the results of our simulations. Although the highest altitude penetrated by the bubble of our simulation presented in this study is only 475 km (see left panel of Fig. 2), far below the altitude 600 km of the ROCSAT-1's orbit, it is reasonable to apply the result of our simulation to explain the IPEI data because of following reasons. Fig. 2 clearly indicates that the penetration depth increases with increasing scale size of the bubble, and in our previous study [27], a bubble with a scale length of 100 km had reached the upper boundary (530 km) of the simulation box, and it would surely have penetrated further if the upper boundary of the simulation box were higher. Therefore, a bubble of scale size several hundred kilometers should be able to penetrate through the altitude of 600 km. When the satellite passes through the IB region of primary bubble-irregularities, it sees the irregular waveforms with the spectral index around $\alpha \approx 2$ down to the scale as small as 90 m. The secondary bubbles (secondary bubbles of $n + 1$ -th generation) with scale smaller than 90 m (approximately) grown from the interior of the primary bubble (secondary bubble of n -th generation) will break into irregular structures at the top walls of the primary bubble (secondary bubble of n -th generation). Since the wall occupies a much smaller area than the interior of the bubble, the satellite will have much higher probability of seeing the smooth waveform than seeing the irregular waveforms of the secondary bubble-irregularities. Therefore, the spectral index sharply decreases from $\alpha \approx 2.7$ to $\alpha \approx 4.2$ » the former must result from seeing the smooth waveforms and irregular waveforms of the secondary bubbles alternatively, and the later results from seeing the smooth waveforms of the secondary bubble-irregularities.

IV-2. Vertical velocity fluctuation

Applying the same procedure of spectral analysis on the time series of vertical velocity v_z (note: not $v_z = \partial_z v_z$) of the same bubble event, we obtain Fig. 10. The left panel (counterpart of Fig. 8) shows the averaged spectral power and the right panel (counterpart of Fig. 9) shows the spectral index as a function of the horizontal wave number. It can be seen that, at long wavelengths ($\lambda > 300$ m), the spectrum is shallow, with spectral index between $\alpha \approx 1$ and $\alpha \approx 2$; at short wavelengths ($\lambda < 90$ m), the spectrum becomes very steep, with spectral index approaching $\alpha \approx 4$. The spectrum characteristics in these two ranges appear somewhat similar to that of the density fluctuation spectrum (comparing with Fig. 8). However, in the wavelengths between 300 m and 90 m, the spectrum is flat with index approaching 0. This characteristic repeatedly appears in ROCSAT-1 data.

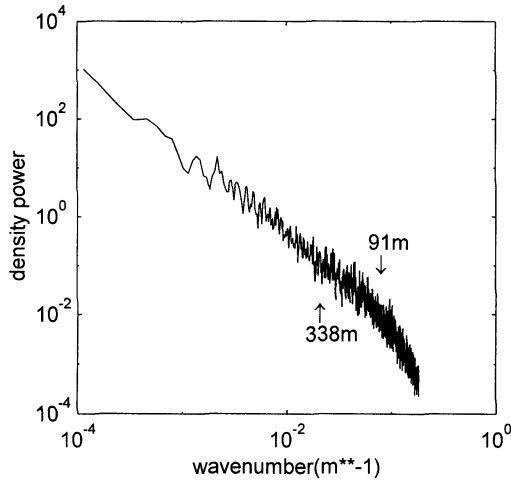


FIG. 8. Averaged power density spectrum of the relative density fluctuation $\zeta n/n$ of one bubble event between 3:25:17 and 3:25:50 on March 28, 1999, observed by IPEI on board the Taiwan satellite ROCSAT-1.

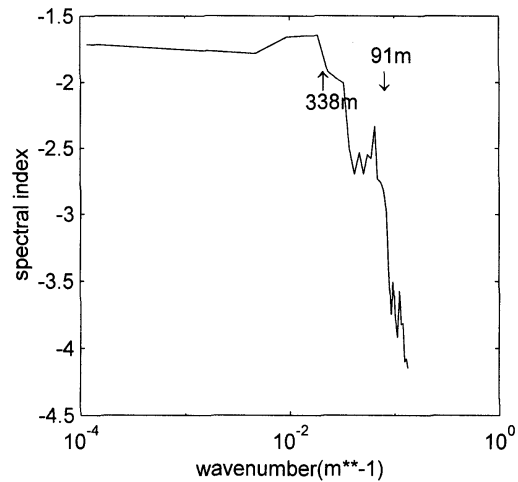


FIG. 9. Spectral index α calculated from Fig. 8 as a function of the wave-number k . The α value of each section is assigned to its first Fourier mode. For example, the spectral index α of the section between $k = 0.0186$ ($\lambda = 338$ m, indicated by the up-arrow) and $k = 0.069$ ($\lambda = 91$ m, indicated by the down-arrow) in Fig. 8 is assigned to $k = 0.0186$.

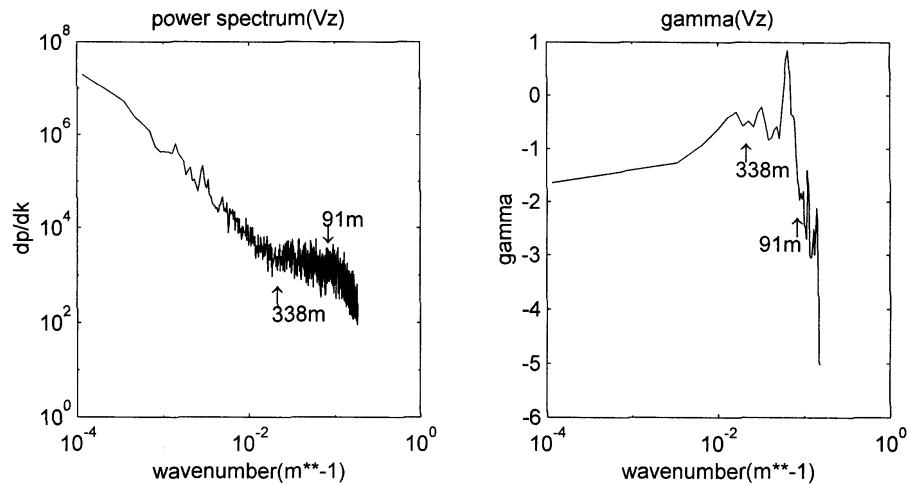


FIG. 10. Corresponding averaged power density spectrum of the vertical drift velocity v_z of the same bubble event of Fig. 8. The left panel (counterpart of Fig. 8) shows the averaged spectral power and the right panel (counterpart of Fig. 9) shows the spectral index as a function of the horizontal wave number.

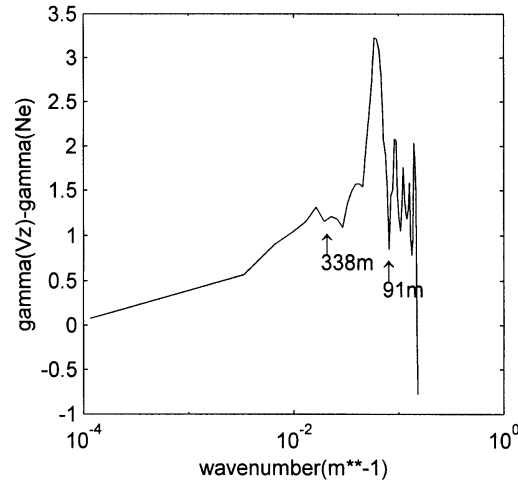


FIG. 11. Wave number dependence of $\gamma(V_z) - \gamma(N_e)$, the difference between the spectral indexes of the vertical drift velocity and density fluctuation, obtained from Fig. 9 and Fig. 10.

To compare the power spectrum of the vertical velocity ($\gamma(V_z)$) with the spectrum of the density fluctuation, the difference between their spectral indexes, $\gamma(V_z) - \gamma(N_e)$, is displayed as a function of horizontal wave number in Fig. 11. At large wave lengths ($\lambda > 300$ m), the difference $\gamma(V_z) - \gamma(N_e)$ gradually increases from 0 to 1 with increasing wave number; at a significant portion of the short wave lengths ($\lambda < 90$ m), the difference $\gamma(V_z) - \gamma(N_e)$ fluctuates between 1 and 2. Since the Boltzmann relationship (with $j \pm V_z j^2 \gg k^2 j \pm n = n j^2$) requires that $\gamma(V_z) - \gamma(N_e) = 2$, it seems that the Boltzmann relationship is not likely to be everything at smaller scales. If anything, the Boltzmann relationship seems to play a more important role at wavelengths smaller than 90 m than at wavelengths longer than 300 m.

V. Summary and discussion

The spectra of equatorial spread F contain much information concerning the physics of nonlinear processes. Rocket and satellite in-situ measurements reveal a common feature that the spectrum has smaller negative index (near $\gamma = -2$) on a scale larger than 100 m, and breaks to a very steep slope ($\gamma \approx -4$) at smaller scales. This feature had not been reproduced previously in any 2-D simulation. Since the ESF wave number spectrum extends at least 6 orders of magnitudes, it is impractical to try to generate the whole spectrum by a single simulation. So we try to study the nonlinear phenomena by combining many simulations at different scales. We have obtained an universal characteristics for the bubble-irregularities regardless of the scale: In the region of density gradient upward (GRT instability region), any perturbation will grow into a bubble welling upward smoothly, when the bubble penetrates into the region of density gradient downward where it is gravitationally stable, the bubble will break into an irregular structure. We may regard the smooth structure and the irregular structures as two phases of a bubble-irregularities system: the smooth structure is in the order-phase and the irregular structure is in the disorder-phase. The breaking of the smooth structure into an irregular structure may be considered as an order-disorder

transition. The horizontal wave number spectra in the region of irregular structures are shallow with spectral index $\frac{1}{4} \leq \beta < 2$, while that in the smooth bubble region are always very steep with spectral index between $\beta \geq 3$ and $\beta \geq 6$, regardless of their scales. In addition, the smooth bubble region (order phase) may be further divided into a growing phase (SB1) and steepening phase (SB2) with spectral indexes in the ranges $\beta \geq 4 \gg \beta \geq 6$ and $\beta \geq 3 \gg \beta \geq 4$, respectively. We believe that this is the origin of the breaking spectrum observed by satellites. When the satellite cuts through the irregular structure of a bubble, it detects a shallow spectrum with spectral index $\frac{1}{4} \leq \beta < 2$; and it will detect a steep spectrum with spectral index between $\beta \geq 3$ and $\beta \geq 6$ when it cuts through the smooth structure of a bubble; when it sees both smooth structure and irregular structures, it will encounter a spectrum with spectral index being somewhere between these two extremes. Another important factor for the existence of the breaking spectrum revealed by our simulations is that the ratio of the height ranges of irregular-structures over smooth-structure decreases with decreasing scale. When the satellite passes through the topside ionosphere, where no smooth structure of primary bubble exists and only irregular structures are available to be detected, we expect shallow spectrum with spectral index $\frac{1}{4} \leq \beta < 2$ at larger scales. Since the thickness of irregular structure decreases with decreasing scale, the irregular structure of small-scale primary bubble-irregularities system will have small probability of being detected. That explains why the shallow spectrum will break at some scale length (probably around 100 m). Also, the density gradient upward region of the interior of the primary bubble-irregularities provides a good environment for a secondary bubble to grow smoothly, and the secondary bubble will most probably break into irregular structures at the vertical wall where the density gradient changes from upward to downward. Since the bubble's wall occupies only a small fraction of the bubble-irregularities system, the probability of seeing the smooth structure is much greater than that of seeing the irregular structure of the secondary bubble-irregularities system. That explains why the spectrum breaks to a very steep slope with index near $\beta \geq 5$ at smaller scales. We have also taken a different scheme from the conventional approach in spectral analysis of satellite or rocket data. First, we limit the data set for the spectral power density calculation strictly to one complete bubble-irregularities event; second, we minimize each section to just 400 modes for the spectral index calculation, to see the dependence of the spectral index on the scale length. Only in this way, we are able to construct a picture for the bubble-irregularities system observed by satellite: When the satellite passes through a bubble-irregularities event in the topside ionosphere, it encounters most likely the disorder-phase of the primary bubble-irregularities and the order-phase of the secondary bubble-irregularities.

The universal characteristics of the horizontal spectra of the electron density fluctuation is obtained by simulations under the condition that the finite ion Larmor radius (FLR) effect is not important. Since the ion Larmor radius is 3 m in the ionosphere, FLR effects on the Rayleigh-Taylor instability will become more and more significant as the scale size of the bubble gets smaller and smaller approaching 3 m. Our numerical model does not include the FLR effect, therefore we do not know how the FLR will affect the GRT instability at different scales. We can only assure that the universal characteristics apply to all the scale sizes of bubbles as long as the FLR effect is negligible. We are not surprised that our numerical model does not result in the Boltzmann relationship since the FLR effect is totally neglected. Two fundamental problems remains to be solved: 1. At what scale length does the FLR start to affect the Rayleigh-Taylor instability? 2. How does the FLR effects affect the Rayleigh-Taylor instability?

The data from the ROCSAT-1 satellite does not present a clear Boltzmann relationship between the horizontal wave-number spectra of $\pm n = \hbar n i$ and $\pm E_x$, it does not completely rule out

a possible existence of the Boltzmann relationship in the transitional scale either. Note that the smallest wavelength in the horizontal wave number spectra of the ROCSAT-1 data analyzed in this paper is 30 m, which is 10 times larger than the ion Larmor radius. The vertical wave-number spectra observed by the rocket experiment of 1990 CRRES/EQUIS campaign [21], reveal that both vector components of the perpendicular electric field (perpendicular to the-magnetic field) are proportional to $\pm n = n$ at wavelengths longer than 300 m but assume a Boltzmann relationship (with $j_{\pm} E j^2 \gg k^2 j_{\pm} n = n j^2$) at smaller scales. In other words, the rocket experiment made by Hysell *et al.* has observed the Boltzmann relationship, but the satellite experiment of ROCSAT-1 neither confirms nor disapproves it. The origin of the break in the slope of the spread F spectrum remains open for further study, both experimentally and numerically.

Acknowledgement

We deeply appreciate IPEI-SDDC of NSPO Taiwan supplying us the raw data we needed. Discussions with Dr. Sunanda Basu and Dr. Santimay Basu were very helpful in clearing up some fundamental problems. This work is supported in part by National Science Council of Taiwan, under the contract number NSC 89-2111-M-008-015-AP9.

References

- [1] A. N. Kolmogorov, Dokl. Akad. NaukSSSR **30**, 301.
- [2] C. Garrett and W. Munk, Geophys. Fluid. Dynamics, **2**, 225 (1972).
- [3] C. Garrett and W. Munk, J. Geophys. Res. **80**, 291 (1975).
- [4] C. Garrett and W. Munk, Ann. Rev. Fluid. Mech. **11**, 339 (1979).
- [5] E. M. Dewan, Science, **204**, 832 (1979).
- [6] T. E. VanZandt, Geophys. Res. Lett. **9**, 575 (1982).
- [7] F. S. Kuo *et al.*, J. Atmos. Terr. Phys. **54**, 31 (1992).
- [8] C. M. Huang, F. S. Kuo, H. Y. Lue and C. H. Liu, J. Atmos. Terr. Phys. **54**, 129 (1992).
- [9] F. S. Kuo and H. Y. Lue, J. Atmos. Terr. Phys. **56**, 1147 (1994).
- [10] M. C. Kelley *et al.*, J. Geophys. Res. **87(A3)**, 1575 (1982).
- [11] P. L. Dyson, J. P. McClure and W. B. Hanson, J. Geophys. Res. **79**, 1479 (1974).
- [12] R. C. Livingston, C. L. Rino, J. P. McClure and W. B. Hanson, J. Geophys. Res. **86**, 2421 (1981).
- [13] M. C. Kelley and J. P. McClure, J. Atmos. Terr. Phys. **43**, 427 (1981).
- [14] H. Kil and R. A. Heelis, J. Geophys. Res. **103**, 3981 (1998).
- [15] S. Y. Su *et al.*, TAO, **10**, 787 (1999).
- [16] E. Costa and M. C. Kelley, J. Geophys. Res. **83**, 4359 (1978).
- [17] C. L. Rino *et al.*, J. Geophys. Res. **86**, 2411 (1981).
- [18] M. C. Kelley *et al.*, J. Geophys. Res. **91**, A5, 5487 (1986).
- [19] J. LaBelle and M. C. Kelley, J. Geophys. Res. **91**, 5504 (1986).
- [20] J. LaBelle, M. C. Kelley and C. E. Seyler, J. Geophys. Res. **91**, 5513 (1986).
- [21] D. L. Hysell *et al.*, J. Geophys. Res. **99**, 8827 (1994a).
- [22] D. L. Hysell, C. E. Seyler and M. C. Kelley, J. Geophys. Res. **99**, 8841 (1994b).
- [23] A. J. Scannapieco and S. L. Ossakow, Geophys. Res. Lett. **3**, 451 (1976).
- [24] M. J. Keskinen, S. L. Ossakow and P. K. Chaturvedi, J. Geophys. Res. **85**, 1775 (1980).
- [25] S. T. Zalessak and S. L. Ossakow, J. Geophys. Res. **85**, 2131 (1980).

- [26] S. Y. Chou and P. S. Kuo, in *Low-Latitude Ionospheric Physics*, Cospar Colloq. Ser., Vol. 7, ed. Pu-Shong Kuo, (Space Program and Res., Paris, 1993), 143-149.
- [27] F. S. Kuo, S. Y. Chou, and S. J. Shan, *J. Geophys. Res.* **103**, 2193 (1998).
- [28] S. Y. Chou and F. S. Kuo, *J. Geophys. Res.* **101**, 17137 (1996).
- [29] J. P. Boris and D. L. Book, *J. Comput. Phys.* **11**, 38 (1973).
- [30] S. T. Zalesak, *J. Comput. Phys.* **31**, 335 (1979).
- [31] D. L. Hysell, Ph.D. thesis, Cornell Univ., Ithaca, N. Y., 1992.
- [32] H. C. Yeh *et al.*, TAO, Supplementary Issue, 19, 1999.